

## IMPACT OF TUBE SURFACE PROPERTIES ON CRYSTALLIZATION FOULING IN FALLING FILM EVAPORATORS FOR SEAWATER DESALINATION

H. Glade<sup>1\*</sup>, A. Stärk<sup>1</sup>, K. Krömer<sup>1</sup>, K. Loisel<sup>2</sup>, K. Odiot<sup>2</sup> and S. Nied<sup>2</sup>

<sup>1</sup> Technical Thermodynamics, University of Bremen, Badgasteiner Str. 1,  
D-28359 Bremen, Germany, [heike.glade@uni-bremen.de](mailto:heike.glade@uni-bremen.de)

<sup>2</sup> BASF SE, D-67056 Ludwigshafen, Germany

### ABSTRACT

Crystallization fouling on heat transfer surfaces is a severe problem and a complex phenomenon in multiple-effect distillation (MED) plants with horizontal tube falling film evaporators for seawater desalination. The choice of tube material affects the wettability, the adhesion forces between surface and deposit as well as the induction time of crystallization fouling.

The effects of surface properties on crystallization fouling from seawater have been investigated in a horizontal tube falling film evaporator in pilot plant scale. Experiments were performed with artificial seawater and various tube materials. The tube surfaces were characterized by measuring surface roughness and contact angles and by determining surface free energies.

The tube materials show qualitative and quantitative differences with respect to scale formation. The interfacial defect model was applied to the system. Spreading coefficients of CaCO<sub>3</sub> scale on the aluminium alloys 5052, 6060 and stainless steel grade 1.4565 were calculated to be higher than those on copper-nickel 90/10 and aluminium brass, but the quantities of CaCO<sub>3</sub> scale measured on the tube surfaces were much lower compared to CuNi 90/10 and Al brass. The application of advanced approaches such as the interfacial defect model depends on the precise knowledge of interfacial free energies which are very difficult to find. However, results suggest that more similar values of the interfacial free energies of heat transfer surface and deposit lead to increased scale formation.

### INTRODUCTION

Multiple-effect distillation (MED) plants with horizontal tube falling film evaporators are commonly used for the production of potable and process water from seawater. In MED plants, crystallization fouling is a severe problem and a complex phenomenon. The scale formed on the heat transfer surfaces reduces the overall heat transfer coefficient. Thus, the efficiency decreases and, above a certain limit, the distillate rate declines. Achieving effective scale control is consequently a major concern of the desalination industry.

There are many factors influencing crystallization fouling. They can be classified into the following three

major categories (Geddert et al., 2009; Zhao and Chen, 2011):

- Operating parameters (surface and bulk temperature, pressure, heat flux, and fluid dynamics like flow velocity, flow regime)
- solution composition (components, concentrations, pH, supersaturation, and suspended particles) and
- heat exchanger characteristics (surface free energy, topography, surface roughness).

In MED plants with horizontal tube falling film evaporators, scale is formed on the outside of the tubes what prevents the use of mechanical cleaning methods such as ball cleaning systems. Effective scale control by suitable anti-scalants requires a profound knowledge of the effects of the operating parameters, the solution composition and the heat exchanger characteristics on scale formation.

Common materials used for heat exchanger tubing in MED plants are copper-nickel 90/10, aluminium brass, titanium grade 2, aluminium alloy 5052 containing between 2.4 and 2.8 % magnesium and highly corrosion-resistant stainless steel grades such as SS 1.4565. The choice of tube material affects the wettability, the adhesion forces between surface and deposit as well as the induction time of crystallization fouling.

Since seawater is a multi-component electrolyte solution, scale formation is caused by co-precipitation of different calcium- and magnesium-containing salts such as calcium carbonate, magnesium hydroxide and calcium sulphate. In former experiments performed in a horizontal tube falling film evaporator with artificial seawater and seawater-based model solutions, Krömer et al. (2015) found that the copper-nickel 90/10 tubes were covered with a two-layer scale comprising a thin, flaky magnesium-rich and calcium-free base layer underneath a thick layer of calcium carbonate crystals in the form of aragonite. Elements like Cu, Ni, Fe, Mn were often detected in the magnesium-rich scale layer. The results suggest that the Mg-rich base layer forms in the early stages and its growth ceases and aragonite crystals start to precipitate once the tube surface is completely covered with the Mg-rich scale layer. Experiments were performed in a wide range of process conditions. With increasing salinity the amount of calcium-containing scale significantly increases. An increase in

temperature and a decrease in wetting rate result in an increase in scale formation. However, the effects of tube material on scale formation and control in horizontal tube falling film evaporators commonly used for seawater desalination have been scarcely investigated. A better understanding of the effects of surface properties on crystallization fouling may help to improve material selection and to mitigate scale formation in heat exchangers.

The main objective of the current research is to contribute to understanding of mixed salt scaling on different tube materials in horizontal tube falling film evaporators under process conditions similar to those in industrial seawater distillers.

In the following, an overview of literature dealing with the influence of interfacial characteristics on crystallization fouling is given. The experimental set-up is presented and the results of the experimental study are discussed.

## INFLUENCE OF INTERFACIAL PROPERTIES ON FOULING

An important parameter influencing interfacial interactions is the interfacial free energy

$$\gamma_{ij} = \left( \frac{\partial G}{\partial A} \right)_{T,p} \quad (1)$$

defined as the total reversible work to create an unit interfacial area at the interface of the phases *i* and *j*. *G* represents the Gibbs free energy of the system, *A* the interfacial area, *T* the temperature and *p* the pressure. In the following,  $\gamma_{ij}$  denotes the interfacial free energy between two adjacent phases *i* and *j*, whereas index “1” corresponds to the adhesive (crystal), index “2” to the substrate (heat transfer surface) and index “3” to the surrounding phase.

So far, no simple correlation between surface free energy or surface roughness and fouling behavior has been confirmed (Zettler et al., 2005; Geddert et al., 2009; Geddert et al., 2011; Liu et al., 2011), but several studies displayed a strong dependence between surface free energy or surface roughness and crystallization fouling. There are a number of contrary reports on the effects of surface energy on fouling behavior (Zhao and Müller-Steinhagen, 2002). Some reports showed that foulants attached preferentially to surfaces with high surface energy, while other reports showed that foulants attached preferentially to surfaces with low surface energy. Numerous studies also indicated there was no relationship between surface energy/wettability and fouling behavior (Zhao and Müller-Steinhagen, 2002). It has long been suspected that poorest foulant adhesion occurs on surfaces with low surface energies and that low energy surfaces were more resistant to build-up of fouling and easier to clean (Zhao and Müller-Steinhagen, 2002; Zettler et al., 2005). Furthermore, it is assumed that increasing surface roughness and increasing quantity of surface pitting result in an increased crystallization fouling (Lei et al., 2011). Many studies were performed with single-salt solutions such as aqueous CaSO<sub>4</sub> or CaCO<sub>3</sub> solutions in pipe flow systems or plate heat exchangers (e.g., Förster and Bohnet, 2000; Lei et al., 2011; Kazi et al., 2012).

Modern anti-fouling strategies are based on approaches increasing the duration of the induction period and, hence, decreasing the adhesive strength between crystals and heat transfer surface (Förster and Bohnet, 2000). The adhesion between crystals and heat transfer surface during the induction period consists of mechanical and molecular interactions. The molecular interactions are described on the basis that dispersive and polar Lifshitz-van der Waals forces are of major importance for the adhesion mechanism. In addition, the Lewis acid-base interactions in polar media and the double layer forces are taken into account (Förster and Bohnet, 2000). In recent studies (Förster et al., 1999; Förster and Bohnet, 1999; Förster and Bohnet, 2000), the interfacial defect model has been analyzed with respect to its ability to identify low-fouling surfaces.

Figure 1 shows interfacial free energies at the boundaries between three adjacent phases. Assuming a spherical crystalline nucleus resting on a heat transfer surface in an aqueous salt solution, the thermodynamic equilibrium is described by means of the contact angle  $\Theta$  between the crystalline deposit and the solid heat transfer surface. The contact angle corresponds to the angle of wetting in liquid/solid/vapour systems. It is the resultant of adhesive and cohesive forces and provides an inverse measure of the wettability of the surface.

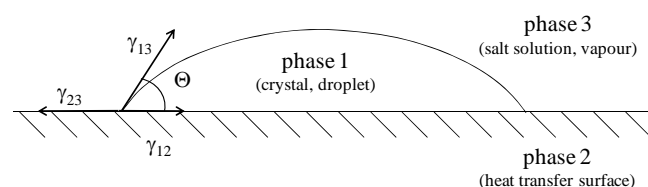


Fig. 1. Interfacial free energies at the boundaries between three phases (Förster and Bohnet, 2000)

Resolving the interfacial free energies in a horizontal direction leads to Young's equation:

$$\gamma_{23} = \gamma_{12} + \gamma_{13} \cos\Theta. \quad (2)$$

The influence of surface material on precipitation fouling can be described by means of the interfacial free energy crystal/heat transfer surface  $\gamma_{12}$ . Several methods for the determination of interfacial free energies can be found in literature. The determination of  $\gamma_{12}$  can be based on a macroscopic approach followed by Lifshitz considering nonpolar and polar interactions found by van der Waals: (a) fluctuating dispersion forces; (b) orienting dipole-dipole interactions; (c) orienting dipole-induced dipole interactions; and hydrogen bonding interactions (van Oss, 1994). The corresponding interfacial energies are characterized by index “LW” (Lifshitz–van der Waals). According to Fowkes (1964) the interfacial free energy can be divided into a dispersive (index “dis”) and a polar (index “pol”) component assumed that van der Waals forces are predominant.

Owens and Wendt (1969) suggested a geometric mean approach to calculate  $\gamma_{12}$  which is mainly applied for nonpolar systems where the ionization potential of adhesive and substrate equals each other:

$$\gamma_{12} = \gamma_{13}^{LW} + \gamma_{23}^{LW} - 2 \left( \sqrt{\gamma_{13}^{dis} \gamma_{23}^{dis}} + \sqrt{\gamma_{13}^{pol} \gamma_{23}^{pol}} \right). \quad (3)$$

Wu (1982) proposed a harmonic mean approach which is applied to low energy systems such as polymers or organic liquids based on the assumption that the polarizabilities of adhesive and substrate are similar:

$$\gamma_{12} = \gamma_{13}^{LW} + \gamma_{23}^{LW} - 4 \left( \frac{\gamma_{13}^{dis} \gamma_{23}^{dis}}{\gamma_{13}^{dis} + \gamma_{23}^{dis}} + \frac{\gamma_{13}^{pol} \gamma_{23}^{pol}}{\gamma_{13}^{pol} + \gamma_{23}^{pol}} \right). \quad (4)$$

For the characterization of high energy systems such as mercury and glass, the geometric harmonic mean approach

$$\gamma_{12} = \gamma_{13}^{LW} + \gamma_{23}^{LW} - 2 \sqrt{\gamma_{13}^{dis} \gamma_{23}^{dis}} - 4 \frac{\gamma_{13}^{pol} \gamma_{23}^{pol}}{\gamma_{13}^{pol} + \gamma_{23}^{pol}} \quad (5)$$

was suggested.

The geometric and harmonic mean methods should be favoured for metallic surfaces since they are state of the art and frequently used in many research areas for the combination of wetting and adhesion (Förster and Bohnet, 2000).

The adhesive strength crystal/heat transfer surface is a function of the spreading coefficient  $\lambda_{12}$  and the interfacial free energy  $\gamma_{23}$  (Förster and Bohnet, 2000):

$$\zeta = C \left( 1 - \frac{\lambda_{12}}{\gamma_{23}} \right)^{-1} \quad (6)$$

with the spreading coefficient of phase 1 on phase 2

$$\lambda_{12} = \gamma_{23} - \gamma_{13} - \gamma_{12}. \quad (7)$$

C refers to the mechanical properties of the system such as the Young's modulus. The spreading coefficient can be interpreted as the difference between the work of adhesion and the work of cohesion per unit surface area. Increasing  $\lambda_{12}$  leads to an improved wettability and, as a consequence, an increase in the adhesive strength  $\zeta$  due to less interfacial defects. Two cases have to be considered:

- (i) The equilibrium of forces according to Young's equation (2) is valid, i.e.  $0^\circ \leq \Theta \leq 180^\circ$ . Spontaneous spreading ( $\Theta = 0^\circ$ ) occurs if  $\lambda_{12} = 0$ . No spreading ( $\Theta = 180^\circ$ ) occurs if  $\lambda_{12} = -2 \gamma_{13}$ .
- (ii) For  $\lambda_{12} > 0$ , the system is not in the state of equilibrium any longer. A positive spreading coefficient means that phase 1 spreads immediately and completely over phase 2.

## EXPERIMENTAL

The experimental studies were carried out in a horizontal tube falling film evaporator in pilot plant scale. The effects of tube material on scale formation were studied by performing experiments with artificial seawater.

### Test Rig

The main part of the test rig is an evaporator fitted with a bank of 6 horizontal tubes arranged below each other. Saturated steam is introduced into the tubes and condensed under vacuum conditions. The test solution is distributed onto the first tube and trickles down by gravity forming a thin film flow over the horizontal tubes. The enthalpy of condensation allows the feed water to be preheated to the boiling point on the upper tube and then part of it to be

evaporated on the lower tubes. A more detailed description of the test rig is given by Krömer et al. (2015).

The pilot plant is equipped with various components for temperature, pressure, and flow rate measurements and control. Therefore, the test rig allows systematic studies by varying the process parameters and simulating process conditions in different stages of industrial MED plants.

### Test Procedure

In order to consider a possible extension of the operating range of multiple-effect distillers towards higher top brine temperatures, experiments were performed at an evaporation temperature exceeding the top brine temperatures currently prevailing in industrial multiple-effect distillers. The experiments were performed at an evaporation temperature of  $t_{EV} = 75^\circ\text{C}$  and a condensation temperature of  $t_{CO} = 80^\circ\text{C}$  inside the tubes. The wetting rate,

$$\Gamma = \frac{\dot{m}}{L} \quad (8)$$

was  $\Gamma = 0.1 \text{ kg}/(\text{s m})$ .

After each test run the inside of the evaporator was cleaned manually with deionized water and with diluted acetic acid solution. The collecting tank for the seawater was cleaned with water jets. The whole circuit was cleaned by flushing with deionized water for several days. For each test run, new tubes were used for the third, fourth and fifth tube from the top of the tube bank because scale layers on these tubes were analyzed (see Section "Chemical and Structural Characterization of the Scales"). The tubes installed on the first, second and sixth position were used twice and then renewed. They were removed from the tube sheets and thoroughly cleaned after the first usage.

### Tube Materials

The tubes can be removed from the tube sheets in order to test different tube materials, to renew the tubes and to analyze the adherent scale. In the experiments, common evaporator tubing materials were used, namely copper-nickel 90/10, aluminium brass, aluminium alloy 5052 containing between 2.4 % and 2.8 % magnesium and stainless steel grade 1.4565 (super-austenitic stainless steel with high corrosion resistance). Additionally, aluminium alloy 6060 containing between 0.35 and 0.60 % magnesium, which is less corrosion resistant than alloy 5052, was used.

The outer diameter of the tubes was  $d_0 = 25 \text{ mm}$  and the effective length was  $L = 453 \text{ mm}$ . As far as available from tube suppliers, the wall thickness of the tubes was adjusted with regard to the different thermal conductivities of the materials in order to have similar heat conduction resistances and heat fluxes and to perform the tests under similar conditions.

The tubes were employed with their typical surface topography as delivered by the tube suppliers and as commonly used in MED plants. The surface roughness was determined using a tactile stylus unit (perthometer). The tube materials, thermal conductivities, wall thicknesses and surface roughnesses are summarized in Table 1.

Table 1. Tube data (outer diameter  $d_0 = 25$  mm, effective length  $L = 453$  mm)

Alloy designation Chemical designation UNS No.	Thermal conductivity / W/(m K) (VDI, 2013)	Wall thickness / mm	Surface roughness $R_a$ / $\mu\text{m}$
<b>CuNi 90/10</b> CuNi10Fe1Mn C70600	52 (20°C) 60 (100°C)	1.0	0.37
<b>Al brass</b> CuZn20Al2As C68700	100 (20°C) 112 (100°C)	2.0	0.38
<b>SS 1.4565</b> X2CrNiMnMoNbN 25-18-5-4 S34565	13 (20-100°C)	0.5	0.16
<b>5052</b> AlMg2.5 A95052	134/140 (0°C) 146 (100°C)	1.25	0.46
<b>6060</b> AlMgSi A96060	200 – 220 (20°C)	1.5	0.15

### Test Solution

In the experiments, artificial seawater based on salt mole fractions for standard artificial seawater as suggested in the formulation by Kester et al. (1967) was used. The composition of artificial seawater is within 1 mg/kg of natural seawater for all the major constituents (Kester et al., 1967). After mixing the salts and stirring, the solution was aerated. The aeration tended to equilibrate the solution with atmospheric gases and removed the excess  $\text{CO}_2$  resulting from the conversion of  $\text{HCO}_3^-$  to  $\text{CO}_3^{2-}$ . The pH of the artificial seawater after aeration was between 8.1 and 8.3.

The salinity of ocean surface waters throughout the world is fairly uniform about 35 g/kg. In areas with a high level of rainfall or river runoff, the salinity is less. In areas with higher rates of evaporation, the salinity is higher, e.g. in the Persian Gulf. In seawater, the relative proportion of the major ions compared to the salinity remains constant (Millero, 2006). Therefore, the artificial seawater used in the experiments is representative for natural seawater. Experiments were performed with artificial seawater having a salinity of 45 g/kg and an ionic strength of  $I = 0.94$  mol/kg simulating, for example, the seawater in the Persian Gulf.

All experiments were performed with 240 liters of artificial seawater for test periods of 4 hours and 50 hours. In previous experiments, different volumes of test solution and time periods were tested. Experiments with 240 liters of test solution were found to be favorable because supersaturation levels are still high enough (Glade et al., 2003; Glade et al., 2005).

### Surface Characterization

In order to differentiate influential factors, the tube surfaces were characterized. The advancing contact angle was measured on top of the tubes using a drop shape analysis (DSA) instrument (KRÜSS, contact angle measurement system G2). A sessile drop is formed on the surface by means of a syringe needle and the volume of the drop is slowly increased. In doing so, the interface migrates

outwards. By means of a CCD camera and a data processing system the image of the liquid droplet is digitized. A contour recognition is initially carried out and afterwards the drop shape is fitted to the contour.

Before measuring the contact angle, the surface was thoroughly cleaned with isopropyl alcohol to remove any deposits, grease, oil, etc..

The surface free energy was determined on the basis of the contact angle measurements with three test liquids, which are shown in Table 2, and Young's equation (2). The solid/liquid interfacial free energy between tube surface and droplet in Young's equation was calculated using the geometric mean approach according to Equation (3).

Table 2. Test liquids and their physical properties used for contact angle measurements

Liquid	Surface free energy / mN/m	Dispersive part / mN/m	Polar part / mN/m
Water	72.8	21.8	51.0
Diiodomethane	50.8	50.8	0
Ethylene glycol	47.7	30.9	16.8

### Chemical and Structural Characterization of the Scales

The crystalline scale layers formed outside the horizontal tubes of the falling film evaporator were analyzed by various methods to obtain chemical, structural, and quantitative information. Scanning electron microscopy (SEM) in combination with energy dispersive X-ray spectroscopy (EDXS) and wide angle X-ray diffraction (XRD) provide qualitative information on structural and chemical characteristics/properties of the scale, especially about composition, crystal structure, crystal size and orientation. The amounts of calcium and magnesium in the scale were detected by inductively coupled plasma atomic emission spectroscopy (ICP-AES). The thickness of the scale layer was measured with a gauge based on the eddy current principle.

Scale thickness was determined on the third tube from the top of the tube bank. The scale of the fourth tube was dissolved in a hot solution of acetic acid and the concentrations of  $\text{Ca}^{2+}$  and  $\text{Mg}^{2+}$  ions in the solution were measured using ICP-AES. Furthermore, the fifth tube was analyzed using SEM, EDXS, and XRD.

### RESULTS

In the following, the contact angles with water and the surface free energies of the different tube materials are shown. Afterwards, the effects of tube material on the composition, structure, and quantity of the scale in horizontal tube falling film evaporators are presented and discussed.

### Contact Angle and Surface Free Energy

The contact angles were measured on top of the tubes. Guilizzoni (2011) experimentally investigated the shape and the contact angle of drops on curved surfaces. Image processing, spline fitting and numerical integration were used to extract the drop contour in a number of cross-sections. The three-dimensional surfaces were visualized

and a simple procedure was proposed to determine the equilibrium contact angle starting from measurements on curved surfaces. A comparison with the results of Guilizzoni (2011) and discussions with different experts in the field of drop shape analysis have shown that the influence of the curved surface is negligible in the present work. Furthermore, all tested tubes had the same diameter and therewith the same curvature which allows a comparison between the materials.

The measured contact angles of water on the tube materials and the surface free energies of the metals calculated on the basis of the geometric mean approach according to Equation (3) are shown in Figure 2. Decreasing contact angles are accompanied by an improved wettability of the surfaces. The order of the contact angles of water on the different metals was found to be alloy 6060 < Al brass < alloy 5052  $\approx$  SS 1.4565 < CuNi 90/10. The results suggest that the wettability of the metals is in the order of 6060 > Al brass > 5052  $\approx$  SS 1.4565 > CuNi 90/10 which complies with the own practical experience except for SS 1.4565 showing the lowest wettability in the pilot plant.

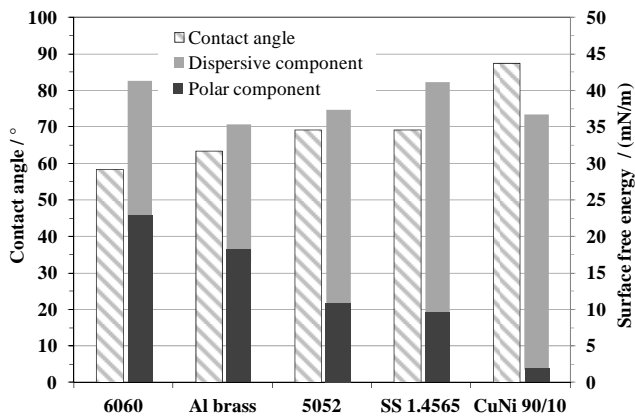


Fig. 2. Contact angles with water and surface free energies of the tube materials

### Effect of Tube Material on Scale Formation

The SEM images in Figure 3 show the scale formed on the surface of the CuNi 90/10 tubes after a test period of 4 hours and 50 hours, respectively. The experiments were performed with artificial seawater having a salinity of 45 g/kg at a high evaporation temperature of 75°C and a wetting rate of 0.1 kg/(s m).

The tube surface is covered mainly with  $\text{CaCO}_3$  (aragonite) and  $\text{Mg}(\text{OH})_2$  (brucite). The flaky brucite forms a thin base layer on the tube surface. Rod-shaped aragonite crystals grew up on this base layer. Some  $\text{CaSO}_4$  crystals were found on the tube surface after a test period of 50 hours.

The SEM images of the scale formed on the surface of the aluminium brass tubes after a test period of 4 hours and 50 hours, respectively, are shown in Figure 4. Similar to the CuNi 90/10 tubes, the aluminium brass tubes were covered with a two-layer scale comprising a thin, flaky magnesium-containing base layer underneath a thick layer of calcium carbonate crystals in the form of aragonite.

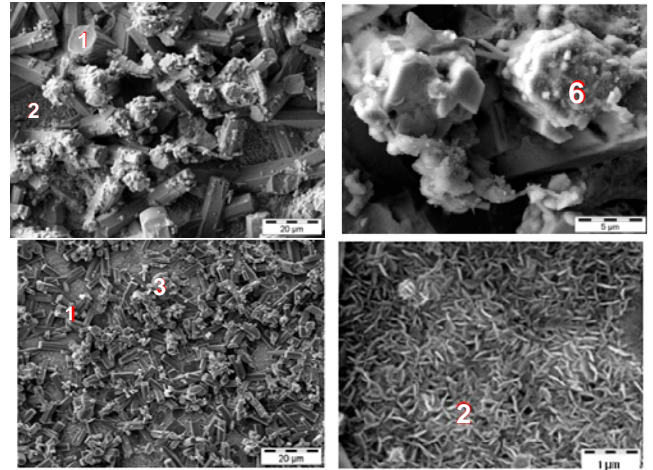


Fig. 3. SEM images showing the CuNi 90/10 tube surface after a test period of 4 h (top row) and 50 h (bottom row); artificial seawater,  $t_{\text{EV}} = 75^\circ\text{C}$ ,  $t_{\text{CO}} = 80^\circ\text{C}$ ,  $S = 45 \text{ g/kg}$ ,  $\Gamma = 0.1 \text{ kg/(s m)}$ : 1-  $\text{CaCO}_3$  (aragonite), 2-  $\text{Mg}(\text{OH})_2$  (brucite), 3-  $\text{CaSO}_4$ , 6- Cu, O-containing scale

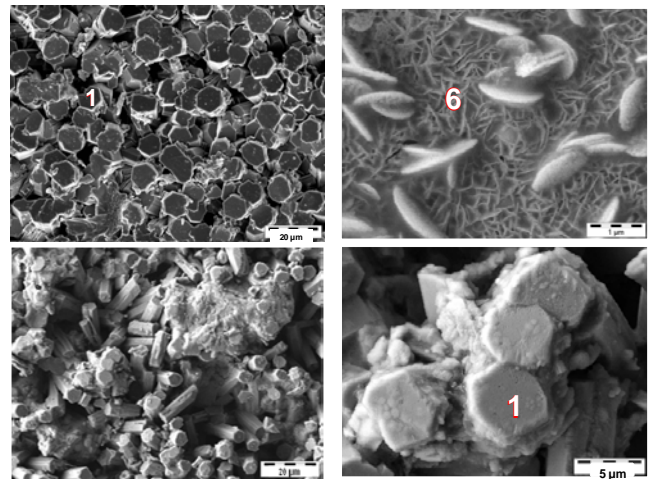


Fig. 4. SEM images showing the Al brass tube surface after a test period of 4 h (top row) and 50 h (bottom row); artificial seawater,  $t_{\text{EV}} = 75^\circ\text{C}$ ,  $t_{\text{CO}} = 80^\circ\text{C}$ ,  $S = 45 \text{ g/kg}$ ,  $\Gamma = 0.1 \text{ kg/(s m)}$ : 1-  $\text{CaCO}_3$  (aragonite), 6- Cu, Zn-containing scale with traces of Mg, Ca

Figure 5 shows the SEM images of the scale formed on the surface of the SS 1.4565 tubes after a test period of 4 hours and Figure 6 illustrates the tube surface after a test period of 50 hours. While the CuNi 90/10, Al brass, alloy 5052 and alloy 6060 tubes showed a relatively uniform scale layer, the scale formed on the tubes made of the stainless steel grade 1.4565 was very unevenly distributed. Some surface areas were densely covered with scale, some areas were only weakly covered and some spots were even almost uncovered, as shown in Figures 5 and 6.

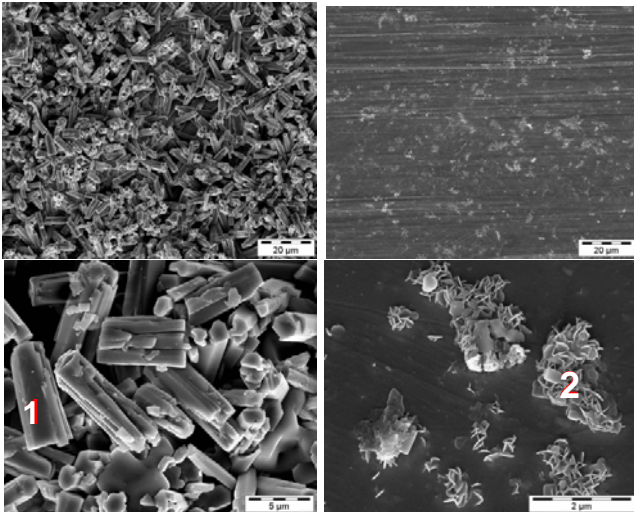


Fig. 5. SEM images showing the SS 1.4565 tube surface after a test period of 4 h; artificial seawater,  $t_{EV} = 75^{\circ}\text{C}$ ,  $t_{CO} = 80^{\circ}\text{C}$ ,  $S = 45 \text{ g/kg}$ ,  $\Gamma = 0.1 \text{ kg/(s m)}$ : 1-  $\text{CaCO}_3$  (aragonite), 2-  $\text{Mg}(\text{OH})_2$  (brucite)

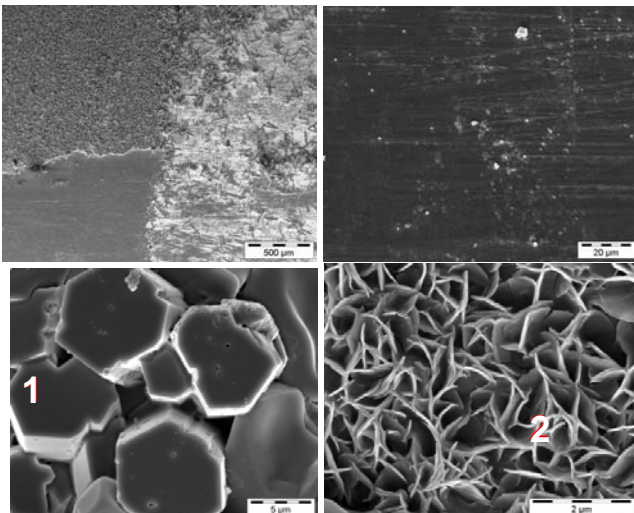


Fig. 6. SEM images showing the SS 1.4565 tube surface after a test period of 50 h; artificial seawater,  $t_{EV} = 75^{\circ}\text{C}$ ,  $t_{CO} = 80^{\circ}\text{C}$ ,  $S = 45 \text{ g/kg}$ ,  $\Gamma = 0.1 \text{ kg/(s m)}$ : 1-  $\text{CaCO}_3$  (aragonite), 2-  $\text{Mg}(\text{OH})_2$  (brucite)

The SEM images in Figure 7 show the scale formed on the surface of the alloy 6060 tubes after a test period of 4 hours and 50 hours, respectively. The tube surface is densely covered with a flaky magnesium-containing scale. Some rod-shaped aragonite crystals grew up on this base layer and some  $\text{CaSO}_4$  crystals were found on the tube surface. Compared to the CuNi 90/10, aluminium brass and SS 1.4565 tube surfaces, a thicker layer of magnesium-containing scale and less  $\text{CaCO}_3$  was found on the 6060 tubes.

Figure 8 shows the SEM images of the scale formed on the surface of the alloy 5052 tubes after a test period of 4 hours and 50 hours, respectively.

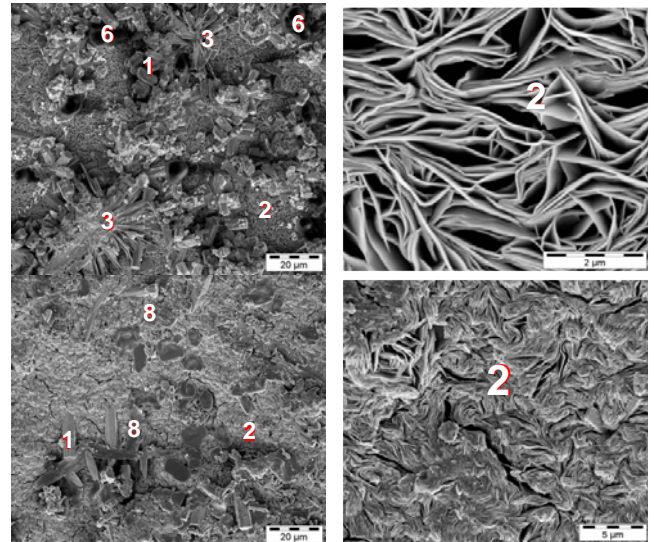


Fig. 7. SEM images showing the alloy 6060 tube surface after a test period of 4 h (top row) and 50 h (bottom row); artificial seawater,  $t_{EV} = 75^{\circ}\text{C}$ ,  $t_{CO} = 80^{\circ}\text{C}$ ,  $S = 45 \text{ g/kg}$ ,  $\Gamma = 0.1 \text{ kg/(s m)}$ : 1-  $\text{CaCO}_3$  (aragonite), 2- Mg, O-containing scale, 3- needle-like Ca, S, O-containing scale, 6- Al, O-containing scale, 8- Al, O, Mg-containing scale

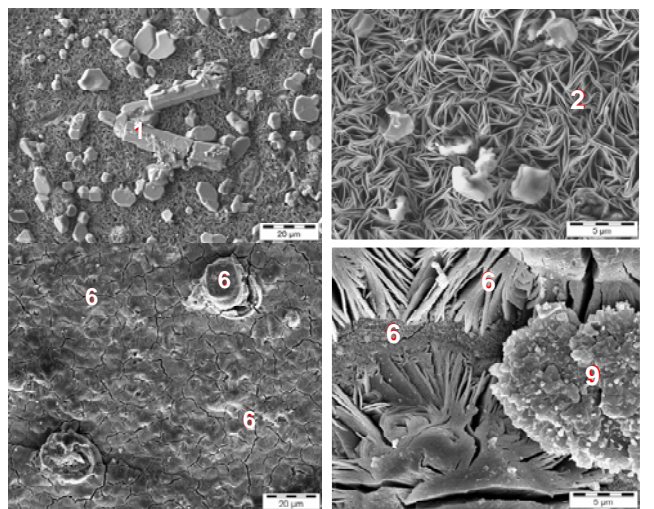


Fig. 8. SEM images showing the alloy 5052 tube surface after a test period of 4 h (top row) and 50 h (bottom row); artificial seawater,  $t_{EV} = 75^{\circ}\text{C}$ ,  $t_{CO} = 80^{\circ}\text{C}$ ,  $S = 45 \text{ g/kg}$ ,  $\Gamma = 0.1 \text{ kg/(s m)}$ : 1-  $\text{CaCO}_3$  (aragonite), 2- Mg, O-containing scale, 6- Mg, O, Al-containing scale, 9- Ca, C, O, Na, Mg, Al-containing deposit

Figure 9 shows the ICP-AES results for the masses of calcium and magnesium per unit tube surface area for the different alloys after test periods of 4 hours and 50 hours. The tube materials show qualitative and quantitative differences with respect to scale formation. After a short test period of 4 hours, most scale was found on the CuNi 90/10 tubes. Less scale was found on the aluminium brass tubes and much less scale formed on the 5052, 6060 and SS 1.4565 tubes. After a test period of 50 hours, the scale quantity found on the CuNi 90/10 tubes was higher than

that found on the SS 1.4565 tubes. The scale quantity on the aluminium brass tubes was similar to the quantity found on the SS 1.4565 tubes. After 50 hours, the lowest scale quantity was found on the 6060 and 5052 tubes. While the magnesium mass per unit tube surface area was low on the CuNi 90/10, Al brass and SS 1.4565 tubes and the quantity of the magnesium-containing scale did not notably change with increasing test period, the magnesium mass in the scale per unit tube surface area was relatively high on the 5052 and 6060 tubes and even increased after 50 hours. However, the quantity of the calcium containing scale was relatively low after 50 hours. The results suggest that the magnesium-containing scale has a higher affinity to the aluminium alloys.

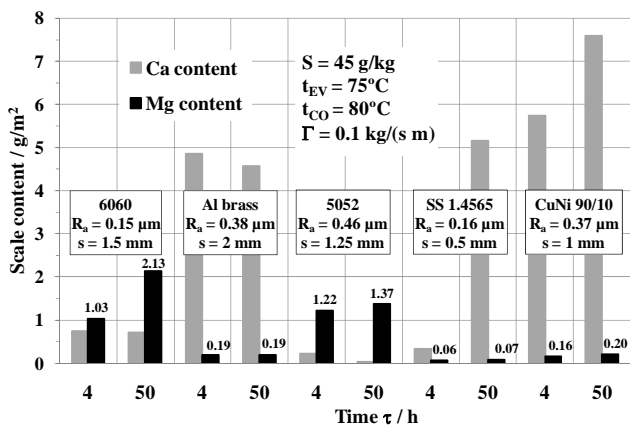


Fig. 9. Effects of tube material on the masses of calcium and magnesium in the scale per unit tube surface area

## DISCUSSION

An energy balance calculation showed that only part of the first tube was needed to heat up the seawater film to evaporation temperature during steady state operation. Due to the evaporation on the tubes below, the seawater concentration increased and the wetting rate decreased by approximately 2.5 %. The film Reynolds number, defined as the wetting rate divided by the dynamic viscosity of the liquid, slightly decreased from  $Re_F = 235$  where evaporation temperature was reached at the top tube to  $Re_F = 230$  at the bottom tube. Slightly increased scale formation from the top tube to the bottom tube was observed which can be attributed to the increased supersaturation and the decreased friction forces. For all experiments, the scale on the fourth tube was analyzed using ICP-AES, as shown in Figure 9. Thus, similar conditions in terms of concentration, wetting rate and film Reynolds number prevailed at the fourth tube in the experiments.

Surface energy is an important property that affects adhesion. In general, a surface having lower surface energy is more stable and less susceptible to adhesion. The higher the surface energy is, the greater is the attraction, and the lower the surface energy is, the weaker are the resulting attractive forces (Sheikholeslami, 2007). As shown in Figures 5 and 6, the crystalline scale on the stainless steel 1.4565 tubes was very unevenly distributed. Some areas

were only weakly covered and some areas were even uncovered. The induction period for crystallization fouling on stainless steel 1.4565 tubes having a relatively high surface free energy, as shown in Figure 2, and showing the lowest wettability in practice might be extended or crystal growth might break off caused by the weak adhesive forces. The anti-adhesive effect of the stainless steel surface may be underlined by the very low friction forces which even slightly decreased from the top tube to the bottom tube.

The polar and dispersive parts of the surface free energies and the total scale quantities after a test period of 4 hours are summarized in Figure 10. The comparison of surface free energy data with scale quantities in Figure 10 yields that there is no simple correlation between the surface free energy or its polar component, respectively, and the fouling behavior.

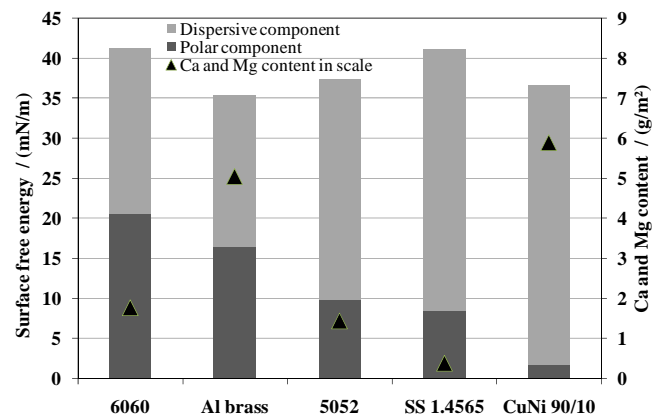


Fig. 10. Calcium and magnesium scale quantities after a test period of 4 hours and surface free energies of different tube materials,  $t_{EV} = 75^\circ\text{C}$ ,  $t_{CO} = 80^\circ\text{C}$ ,  $S = 45 \text{ g/kg}$ ,  $\Gamma = 0.1 \text{ kg/(s m)}$

Kazi et al. (2012) reported that the extent of fouling on different metal surfaces increases with increasing thermal conductivity of the metal (copper > aluminium > brass > stainless steel). In the current research, the wall thickness of the tubes was adjusted, as far as available from tube suppliers, with regard to the different thermal conductivities of the materials in order to have similar heat conduction resistances and heat fluxes and to perform the tests under similar conditions. Thus, considerable effects of the different thermal conductivities can be excluded.

In the present study, the effects of surface roughness on scale formation were not investigated. The tubes were used as delivered by the suppliers with a relatively low surface roughness, as shown in Table 1. It is assumed that rough surfaces may act as nucleation sites reducing the induction period (Keysar et al., 1994; Sheikholeslami, 2007). Keysar et al. (1994) reported that a consequence of the enhanced nucleation on a rough substrate surface is the formation of a stronger adhesive bond. They showed that metal surface roughness exerted a significant effect on the tenacity of calcite deposit on mild steel. The tensile stress required to remove the bond of a calcite deposit adhering to a rough metal surface ( $R_a$  between 18 and 24  $\mu\text{m}$ ) was found to be 30 times higher than that required to remove the bond of a

calcite deposit adhering to a smooth surface ( $R_a$  between 0.1 to 0.15  $\mu\text{m}$ ). However, Al-Anezi et al. (2008) demonstrated that a stainless steel sample with  $R_a = 0.33 \mu\text{m}$  had the lowest adhesion while a sample with  $R_a = 0.038 \mu\text{m}$  was secondary and a sample with  $R_a = 0.12 \mu\text{m}$  had the highest adhesion. Förster and Bohnet (2000) proposed a two-dimensional surface texture parameter and showed that the induction time is proportional to the surface texture parameter. Liu et al. (2011) found that the influence of surface roughness on adhesion is limited. They confirmed that there is no simple relationship between surface roughness and adhesion. The authors proposed that the effect of roughness on adhesion can be attributed to the effect of the formation of a “transitional interface” via corrosion or oxidation. Surfaces with a large or small roughness show a relative good corrosion resistance. Surfaces with a medium roughness are more prone to the formation of a “transitional interface” which connects the fouling and the matrix surface.

In the present study, aluminium alloy 6060 and SS 1.4565 having the lowest surface roughness as well as aluminium alloy 5052 having the highest roughness showed low scale formation after 4 hours. An overlap of surface roughness and energetic effects complicates a simple interpretation. Moreover, it is likely that corrosion products on the copper alloys accelerate scale formation as reported in literature (e.g., Alahmad, 2008). A thin layer of copper oxide, which forms on the tube surface and serves as a protective layer, influences the interfacial free energy of the substrate and, thus, the molecular interactions and the adhesion. As proposed by Liu et al. (2011), corrosion or oxidation products of the metal matrix may form a “transitional interface” which connects the fouling and the matrix surface.

Since the crystalline deposit also influences molecular interaction at the interface crystal/heat transfer surface, it has to be taken into account. The interfacial defect model (Förster and Bohnet, 1999; Förster et al., 1999; Förster and Bohnet, 2000) was applied to the system in order to analyze its ability to predict the scaling tendency on different tube materials in desalination systems.

The spreading coefficient  $\lambda_{12}$  of  $\text{CaCO}_3$  on the respective tube material was determined with Equation (7). According to Equations (3) to (5), the interfacial free energy  $\gamma_{12}$  can be calculated if  $\gamma_{23}^{\text{pol/dis}}$  and  $\gamma_{13}^{\text{pol/dis}}$  are accessible. For  $\gamma_{23}^{\text{pol}}$  and  $\gamma_{23}^{\text{dis}}$ , data shown in Figure 2, which are based on wetting experiments and the drop shape analysis method, were used. Data for the interfacial free energy  $\gamma_{13}$  of  $\text{CaCO}_3$  scale, especially for the polar and dispersive components  $\gamma_{13}^{\text{pol}}$  and  $\gamma_{13}^{\text{dis}}$ , are very difficult to find. In order to receive surface free energy characteristics of  $\text{CaCO}_3$  scale, wetting experiments were performed using the DSA method. The interfacial free energy between  $\text{CaCO}_3$  scale and droplet in Young’s equation was calculated using the geometric mean approach according to Equation (3). Additionally, the polar and dispersive components  $\gamma_{13}^{\text{pol}}$  and  $\gamma_{13}^{\text{dis}}$  of the interfacial free energy of

$\text{CaCO}_3$  taken from a database (KRÜSS, 2015) were used. Data for the polar and dispersive components of the interfacial free energy of  $\text{CaCO}_3$  are summarized in Table 3.

Table 3. Interfacial free energy of  $\text{CaCO}_3$

$\text{CaCO}_3$	Surface free energy $\gamma_{13}$ / mN/m	Polar component $\gamma_{13}^{\text{pol}}$ / mN/m	Dispersive component $\gamma_{13}^{\text{dis}}$ / mN/m
Own experimental data	27.29	8.44	18.85
Data from database (KRÜSS, 2015)	33.10	10.20	22.90

The calculated spreading coefficient  $\lambda_{12}$  of  $\text{CaCO}_3$  on the respective tube material and the measured calcium content in the scale after a test period of 4 hours are depicted in Figure 11. Except for the spreading coefficient of  $\text{CaCO}_3$  on CuNi 90/10 based on the surface free energy data of  $\text{CaCO}_3$  taken from the database, the spreading coefficients are positive which indicates that phase 1 spreads immediately and completely over phase 2. The spreading coefficients for the alloys 5052, 6060 and SS 1.4565 were calculated to be higher than for CuNi 90/10 and Al brass, but the quantities of  $\text{CaCO}_3$  scale measured on the tube surface were much lower compared to CuNi 90/10 and Al brass.

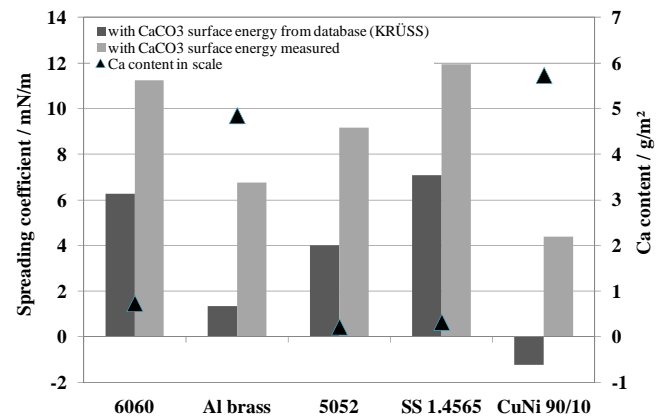


Fig. 11. Calcium scale quantities after a test period of 4 h and spreading coefficients of  $\text{CaCO}_3$  on the respective tube material calculated with surface free energy data  $\gamma_{13}$  of  $\text{CaCO}_3$  taken from a database (KRÜSS, 2015) and based on own measurements,  $t_{\text{EV}} = 75^\circ\text{C}$ ,  $t_{\text{CO}} = 80^\circ\text{C}$ ,  $S = 45 \text{ g/kg}$ ,  $\Gamma = 0.1 \text{ kg/(s m)}$

For scale formation on polymer surfaces, Dreiser and Bart (2014) and Dreiser et al. (2015) showed that scale quantity strongly depends on the interfacial free energy difference ( $\gamma_{23} - \gamma_{13}$ ) between heat transfer surface and deposit. More similar values of the interfacial free energies of heat transfer surface and deposit led to increased scale formation. Dreiser et al. (2015) reported that a lower interfacial free energy difference results in stronger interactions, which implicates both a shorter induction period and a higher amount of final scale deposit. To mitigate scaling,

high interfacial differences ( $\gamma_{23} - \gamma_{13}$ ) should be achieved in heat transfer surface design.

The difference ( $\gamma_{23} - \gamma_{13}$ ) of interfacial free energies between heat transfer surface and  $\text{CaCO}_3$  deposit and the calcium content in the scale after a test period of 4 hours are shown in Figure 12. The interfacial free energy of  $\text{CaCO}_3$  was assumed to be  $\gamma_{13} = 27.29$  mN/m as given in Table 3.

The interfacial free energy differences between Al brass and  $\text{CaCO}_3$  and between CuNi 90/10 and  $\text{CaCO}_3$  are notably lower and calcium scale quantities are considerably higher compared to alloy 6060 and SS 1.4565. As shown in Figure 12, a trend is visible that more similar values of the interfacial free energies of heat transfer surface and deposit lead to increased scale formation.

It has to be noted that the application of advanced approaches such as the interfacial defect model depends on the precise knowledge of interfacial free energies. The interfacial free energies of the heat transfer surfaces are difficult to measure. Surface roughness and surface heterogeneity play an important role. It is even more difficult to find reliable data for the interfacial free energy of the adhesive, namely  $\text{CaCO}_3$  or  $\text{Mg}(\text{OH})_2$  scale. In particular, the porosity of the scale makes it complicated to measure interfacial free energies.

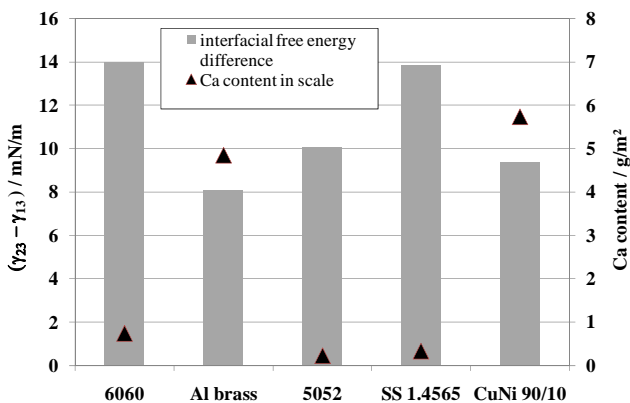


Fig. 12. Calcium scale quantities after a test period of 4 h and interfacial free energy differences between heat transfer surface and  $\text{CaCO}_3$  scale calculated with  $\text{CaCO}_3$  surface free energy data based on own measurements,  $t_{EV} = 75^\circ\text{C}$ ,  $t_{CO} = 80^\circ\text{C}$ ,  $S = 45$  g/kg,  $\Gamma = 0.1$  kg/(s m)

Furthermore, the co-precipitation of calcium- and magnesium-containing salts plays an important role. Due to the complexity of crystallization fouling, research has mainly been restricted to single-salt precipitation. The SEM images show that the tube surfaces are covered with a two-layer scale comprising a thin, flaky magnesium-rich and calcium-free base layer underneath a thick layer of calcium carbonate crystals in the form of aragonite. The results suggest that the Mg-rich base layer forms in the early stages and its growth ceases and aragonite crystals start to precipitate once the tube surface is completely covered with the Mg-rich scale layer. It is conceivable that some tube materials promote the formation of magnesium-containing scale, e.g., the magnesium-containing aluminium alloys,

which in turn influences the precipitation of calcium carbonate scale. The interfacial interactions between the tube surface and  $\text{Mg}(\text{OH})_2$  crystals and the interactions between  $\text{Mg}(\text{OH})_2$  and  $\text{CaCO}_3$  crystals should be taken into account.

Moreover, the use of the geometric or harmonic means based only on van der Waals forces for the calculation of  $\gamma_{12}$  does not account for polar interactions due to the presence of polar media (e.g., water). These electron donor-electron acceptor interactions are explained using the Lewis acid-base theory (Förster and Bohnet, 2000). According to van Oss (1994), the interfacial free energy  $\gamma_{ij}$  can be calculated as a function of a Lifshitz-van der Waals component (index “LW”) and a Lewis acid-base component (index “AB”):

$$\gamma_{ij} = \gamma_{ij}^{\text{LW}} + \gamma_{ij}^{\text{AB}} \quad (9)$$

whereas  $\gamma_{ij}^{\text{AB}}$  comprises an electron acceptor (index “+”) and an electron donor (index “-“) component:

$$\gamma_{ij}^{\text{AB}} = 2 \sqrt{\gamma_{ij}^+ \gamma_{ij}^-} \quad (10)$$

In future research work, a more detailed description of the influence of interfacial interactions considering co-precipitation of magnesium- and calcium-containing salts as well as considering copper oxides on copper alloys should be applied to the system in order to predict the scaling tendency on different tube materials in desalination systems.

## CONCLUSIONS

The effects of tube surface properties on scale formation were studied in a horizontal tube falling film evaporator in pilot plant scale using artificial seawater under conditions near to those in multiple-effect distillation plants for seawater desalination.

1. After a short test period of 4 hours, the scale quantity on the tube materials was in the order of  $\text{CuNi 90/10} > \text{Al brass} \gg \text{alloy 6060} > \text{alloy 5052} > \text{SS 1.4565}$ . After a test period of 50 hours, the scale quantity was in the order of  $\text{CuNi 90/10} > \text{SS 1.4565} \approx \text{Al brass} > \text{alloy 6060} > \text{alloy 5052}$ .
2. While the magnesium mass per unit tube surface area was low on the CuNi 90/10, Al brass and SS 1.4565 tubes and the quantity of the magnesium-containing scale did not notably change with increasing test period, the magnesium mass in the scale per unit tube surface area was relatively high on the tubes made of aluminium alloys 6060 and 5052. However, the quantity of the calcium containing scale was relatively low after 50 hours. The results suggest that the magnesium-containing scale has a higher affinity to the aluminium alloys.
3. Results suggest that there is no simple correlation between surface free energy and fouling behavior. A correlation cannot be based on the surface properties of the heat transfer surface, only. The adjacent crystalline deposit has to be taken into account.
4. The interfacial defect model was applied to the system. Spreading coefficients of  $\text{CaCO}_3$  scale on the alloys

5052, 6060 and SS 1.4565 were calculated to be higher than those on CuNi 90/10 and Al brass, but the quantities of CaCO<sub>3</sub> scale measured on the tube surfaces were much lower compared to CuNi 90/10 and Al brass. The application of advanced approaches such as the interfacial defect model depends on the precise knowledge of interfacial free energies which are very difficult to find.

5. However, results suggest that more similar values of the interfacial free energies of heat transfer surface and deposit lead to increased scale formation.
6. In future research work, a more detailed approach of the influence of interfacial interactions considering co-precipitation of magnesium- and calcium-containing salts as well as considering copper oxides on copper alloys should be applied to the system.

## NOMENCLATURE

A	interfacial area, m <sup>2</sup>
d	tube diameter, m
G	Gibbs free energy, J
I	ionic strength, mol/kg
L	tube length, m
$\dot{m}$	mass flow rate, kg/s
p	pressure, Pa
R <sub>a</sub>	arithmetic average surface roughness, $\mu\text{m}$
Re <sub>F</sub>	film Reynolds number, -
S	salinity, g/kg
s	wall thickness, m
T	temperature, K
t	temperature, °C
$\Gamma$	wetting rate, kg/(s m)
$\gamma_{ij}$	interfacial free energy between phases i and j, N/m
$\zeta$	adhesive strength, N/m <sup>2</sup>
$\Theta$	contact angle, °
$\lambda_{ij}$	spreading coefficient of phase i on phase j, N/m

## Subscript

1	adhesive phase
2	substrate phase
3	surrounding phase
AB	Lewis acid-base component
CO	condensation
dis	dispersive component
EV	evaporation
i	phase i
j	phase j
LW	Lifshitz-van der Waals component
o	outer
pol	polar component
+	electron acceptor
-	electron donor

## REFERENCES

Alahmad, M., 2008, Factors affecting scale formation in sea water environments – An experimental approach, *Chemical Engineering & Technology*, Vol. 31, pp. 149-156.

Al-Anezi, K., Johnson, D.J., and Hilal, N., 2008, An atomic force microscope study of calcium carbonate

adhesion to desalination process equipment: effect of anti-scale agent, *Desalination*, Vol. 220, pp. 359-370.

Dreiser, C., and Bart, H.-J., 2014, Mineral scale control in polymer film heat exchangers, *Applied Thermal Engineering*, 65, pp. 524-529.

Dreiser, C., Krätz, L.J., and Bart, H.-J., 2015, Kinetics and quantity of crystallization fouling on polymer surfaces: Impact of surface characteristics and conditions, *Heat Transfer Engineering*, Vol. 36, pp. 715-720.

Förster, M., Augustin, W., and Bohnet, M., 1999, Influence of the adhesion force crystal/heat exchanger surface on fouling mitigation, *Chemical Engineering and Processing*, Vol. 38, pp. 449-461.

Förster, M., and Bohnet, M., 1999, Influence of the interfacial free energy crystal/heat transfer surface on the induction period during fouling, *Int. J. Therm. Sci.*, Vol. 38, pp. 944-954.

Förster, M., and Bohnet, M., 2000, Modification of molecular interactions at the interface crystal/heat transfer surface to minimize heat exchanger fouling, *International Journal of Thermal Science*, Vol. 39, 697-708.

Fowkes, F.M., 1964, Dispersion force contribution to surface and interfacial tensions, contact angles and heats of immersion, in: *Advances in Chemistry Series 43*, Am. Chem. Soc., Washington, pp. 99-111.

Geddert, T., Bialuch, I., Augustin, W., and Scholl, S., 2009, Extending the induction period of crystallization fouling through surface coating, *Heat Transfer Engineering*, Vol. 30, pp. 868-875.

Geddert, T., Augustin, W., and Scholl, S., 2011, Induction time in crystallization fouling on heat transfer surfaces, *Chemical Engineering and Technology*, Vol. 34, pp. 1303-1310.

Glade, H., Hermersdorf, M., Ulrich, J., Essig, M., Rieger J., and Brodt, G., 2003, Scaling in Multiple-Effect Distillers: New Approach to Study Mechanisms and Control, *Proc. IDA World Congress on Desalination and Water Reuse 2003*, Bahamas.

Glade, H., Wildebrand, C., Will, S., Essig, M., Rieger, J., Büchner, K.-H., and Brodt, G., 2005, Pilot Plant Investigations on Scale Formation and Control in Multiple-Effect Distillers, *Proc. IDA World Congress on Desalination and Water Reuse 2005*, Singapore.

Guilizzoni, M., 2011, Drop shape visualization and contact angle measurement on curved surfaces, *Journal of Colloid and Interface Science*, Vol. 364, pp. 230-236.

Kazi, S.N., Duffy, G.G., and Chen, X.D., 2012, Fouling and fouling mitigation on heated metal surfaces, *Desalination*, Vol. 288, pp. 126-134.

Kester, D.R., Duedall, I. W., Connors, D. N., and Pytkowicz, R. M., 1967, Preparation of artificial seawater, *Limnology and Oceanography*, Vol. 12, pp. 176-179.

Keysar S., Semiat R., Hasson D. and Yahalom Y., 1994, Effect of surface roughness on the morphology of calcite crystallizing on mild steel. *Journal of Colloid and Interface Science*, Vol. 162, pp. 311-319.

Krömer, K., Will, S., Loisel, K., Nied, S., Detering, J., Kempter, A., and Glade, H., 2015, Scale formation and mitigation of mixed salts in horizontal tube falling film

evaporators for seawater desalination, *Heat Transfer Engineering*, Vol. 36, pp. 750-762.

KRÜSS GmbH, Hamburg, Germany, 2015, *Information Database (KIDB)*, <http://www.kruss.de/de/service/schulung-theorie/informationsdatenbank/ueberblick/>, retrieved May 2015.

Lei, C., Peng, Z., Day, T., Yan, X., Bai, X., and Yuan, C., 2011, Experimental observation of surface morphology effect on crystallization fouling in plate heat exchangers, *International Communications in Heat and Mass Transfer*, Vol. 38, pp. 25-30.

Liu, Y., Zou, Y., Zhao, L., Liu, W., and Cheng, L., 2011, Investigation of adhesion of CaCO<sub>3</sub> crystalline fouling on stainless steel surfaces with different roughness, *International Communications in Heat and Mass Transfer*, Vol. 38, pp. 730-733.

Millero, F. J., 2006, *Chemical Oceanography*, 3<sup>rd</sup> ed., CRC Press, Boca Raton.

Owens, D.K., and Wendt, 1969, Estimation of surface energy, *Journal of Applied Polymer Science*, Vol. 13, pp. 1741-1747.

Sheikholeslami, R., 2007, *Fouling in Membranes and Thermal Units. A Unified Approach – Its Principles, Assessment, Control and Mitigation*, Desalination Publications, L'Aquila.

van Oss, C. J., 1994, *Interfacial Forces in Aqueous Media*, Marcel Dekker, New York.

VDI e.V. (ed.), 2013, *VDI-Wärmeatlas*, 11th edition, Springer-Verlag, Berlin, Heidelberg, D6.1, pp. 629-645.

Wu, S., 1982, *Polymer Interface and Adhesion*, Marcel Dekker, New York.

Zettler, H.U., Weiß, M., Zhao, Q., and Müller-Steinhagen, H., 2005, Influence of surface properties and characteristics on fouling in plate heat exchangers, *Heat Transfer Engineering*, Vol. 26, pp. 3-17.

Zhao, Q., and Müller-Steinhagen, H., 2002, Intermolecular and adhesion forces of deposits on modified heat transfer surfaces, *Proc. of the 4th International Conference on Heat Exchanger Fouling, Fundamental Approaches & Technical Solutions*, Davos, July 8-13, 2001. In: PUBLICO Publications, Germany, 2002, pp. 41-46.

Zhao, X., and Chen, X.D., 2011, A critical review of basic crystallography to salt crystallization fouling in heat exchangers, *Proc. of International Conference on Heat Exchanger Fouling and Cleaning 2011*, Crete Island, Greece.